Synthesis of crystals with a programmable kinetic barrier to nucleation

Rebecca Schulman* and Erik Winfree*†‡

Departments of *Computation and Neural Systems and †Computer Science, California Institute of Technology, Pasadena, CA 91125

Edited by Alan R. Fersht, University of Cambridge, Cambridge, United Kingdom, and approved July 19, 2007 (received for review February 16, 2007)

A central goal of chemistry is to fabricate supramolecular structures of defined function and composition. In biology, control of supramolecular synthesis is often achieved through precise control over nucleation and growth processes: A seed molecule initiates growth of a structure, but this growth is kinetically inhibited in the seed's absence. Here we show how such control can be systematically designed into self-assembling structures made of DNA tiles. These structures, "zig-zag ribbons," are designed to have a fixed width but can grow arbitrarily long. Under slightly supersaturated conditions, theory predicts that elongation is always favorable but that nucleation rates decrease exponentially with increasing width. We confirm experimentally that although ribbons of different widths have similar thermodynamics, nucleation rates decrease for wider ribbons. It is therefore possible to program the nucleation rate by choosing a ribbon width. The presence of a seed molecule, a stabilized version of the presumed critical nucleus, removes the kinetic barrier to nucleation of a ribbon. Thus, we demonstrate the ability to grow supramolecular structures from rationally designed seeds, while suppressing spurious nucleation. Control over DNA tile nucleation allows for proper initiation of algorithmic crystal growth, which could lead to the high-yield synthesis of micrometer-scale structures with complex programmed features. More generally, this work shows how a self-assembly subroutine can be initiated.

algorithmic self-assembly | DNA nanotechnology | self-assembly | supramolecular chemistry

Biology demonstrates how self-assembly can create sophisticated organization on the molecular scale. The fundamental challenge in engineering a self-assembled object is that its molecular components must themselves contain the information needed to guide self-assembly.

Controlling the nucleation of a self-assembled object is the first step in controlling the self-assembly process, as exemplified by the formation of actin networks (1, 2), the growth of microtubules on the centrosome (3), and the assembly of bacterial flagella (4). These systems avoid the difficulty of controlling homogeneous (unseeded) nucleation by relying on heterogeneous (seeded) nucleation: Growth is rare except in the presence of a seed molecule, from which it proceeds with little or no kinetic barrier. Here we demonstrate a general strategy for designing self-assembled molecular structures whose nucleation is controlled by a seed. We use programmable DNA tiles to create a series of seeded "zig-zag ribbons" that have increasing kinetic barriers to homogeneous nucleation.

DNA tiles (5, 6) are a general-purpose nanoscale construction material. A DNA tile consists of multiple, interwoven strands that form double helices connected by "crossover points" (Fig. 1*a*). Tiles bind to each other when their single-stranded ("sticky") ends hybridize (Fig. 1*b*) and can assemble into extended structures, including one- and two-dimensional crystals (7–10). Tile interactions are programmed by design of tile sticky ends: Complementary sticky ends hybridize, whereas noncomplementary sticky ends are unlikely to interact. Under slightly supersaturated conditions, where the attachment of a tile to a crystal by two or more sticky ends is favorable but attachment by just one sticky end is unfavorable, in principle it is possible to program complex assembly processes (11).

We have constructed sets of DNA tiles that form ribbons of particular widths. Ribbon assembly proceeds in two phases: nucleation and growth. Under slightly supersaturated conditions, homogeneous nucleation requires both favorable and unfavorable tile attachments. In contrast, growth requires only favorable monomer tile addition reactions and proceeds quickly at both ends of a ribbon along a zig-zag path (Fig. 1 *c* and *d*). Design of nucleation and growth pathways is possible because, under slightly supersaturated conditions, attachment by two (or more) sticky end bonds is favorable, whereas attachment by a single bond is unfavorable. This makes it possible to design the height of the barrier to homogeneous nucleation: The number of unfavorable attachments required for nucleation is the width of a ribbon (in tiles) minus 1. Theoretically, increasing the number of required unfavorable reactions can exponentially reduce the rate of nucleation (12).

In this article, we describe the design and synthesis of ribbons that are three, four, five, and six tiles wide, which are denoted ZZ3–ZZ6. Each ribbon forms as designed and has a significant kinetic barrier to homogeneous nucleation. Measurements of ribbon growth show that nucleation rates are lower for wider ribbons under slightly supersaturated conditions. We then synthesize a seed molecule for ZZ4 ribbons and show that the kinetic barrier to nucleation is greatly reduced in its presence.

Results and Discussion

Tile and Ribbon Structure. Tiles were designed and characterized according to established protocols [see supporting information (SI) *Appendix S1*]. To verify that the tiles assembled into ribbons, the component strands of each ribbon were mixed together at 100 nM (per strand) and annealed from 90° to 20°C over 20 h in a PCR machine. Atomic force microscopy (AFM) of each sample predominantly showed the desired structures (Fig. 2). Most ribbons were micrometers (hundreds of tile layers) long, suggesting that the formation of new ribbons (nucleation) was much slower than the growth of existing ribbons. To establish that annealing is necessary to produce long ribbons, we mixed preformed ZZ4 tiles at room temperature, at which nucleation is presumed to be fast, and let them sit for 20 h. Few ribbons longer than 10 tile layers were observed (see *SI Appendix S2*).

Homogeneous Nucleation Rates. We used 260-nm spectroscopy to measure the rate and temperature dependence of zig-zag ribbon

Author contributions: R.S. and E.W. designed research; R.S. performed research; R.S. and E.W. analyzed data; and R.S. and E.W. wrote the paper.

The authors declare no conflict of interest.

This article is a PNAS Direct Submission.

Freely available online through the PNAS open access option.

Abbreviation: AFM, atomic force microscopy.

‡To whom correspondence should be addressed. E-mail: winfree@dna.caltech.edu.

This article contains supporting information online at www.pnas.org/cgi/content/full/0701467104/DC1.

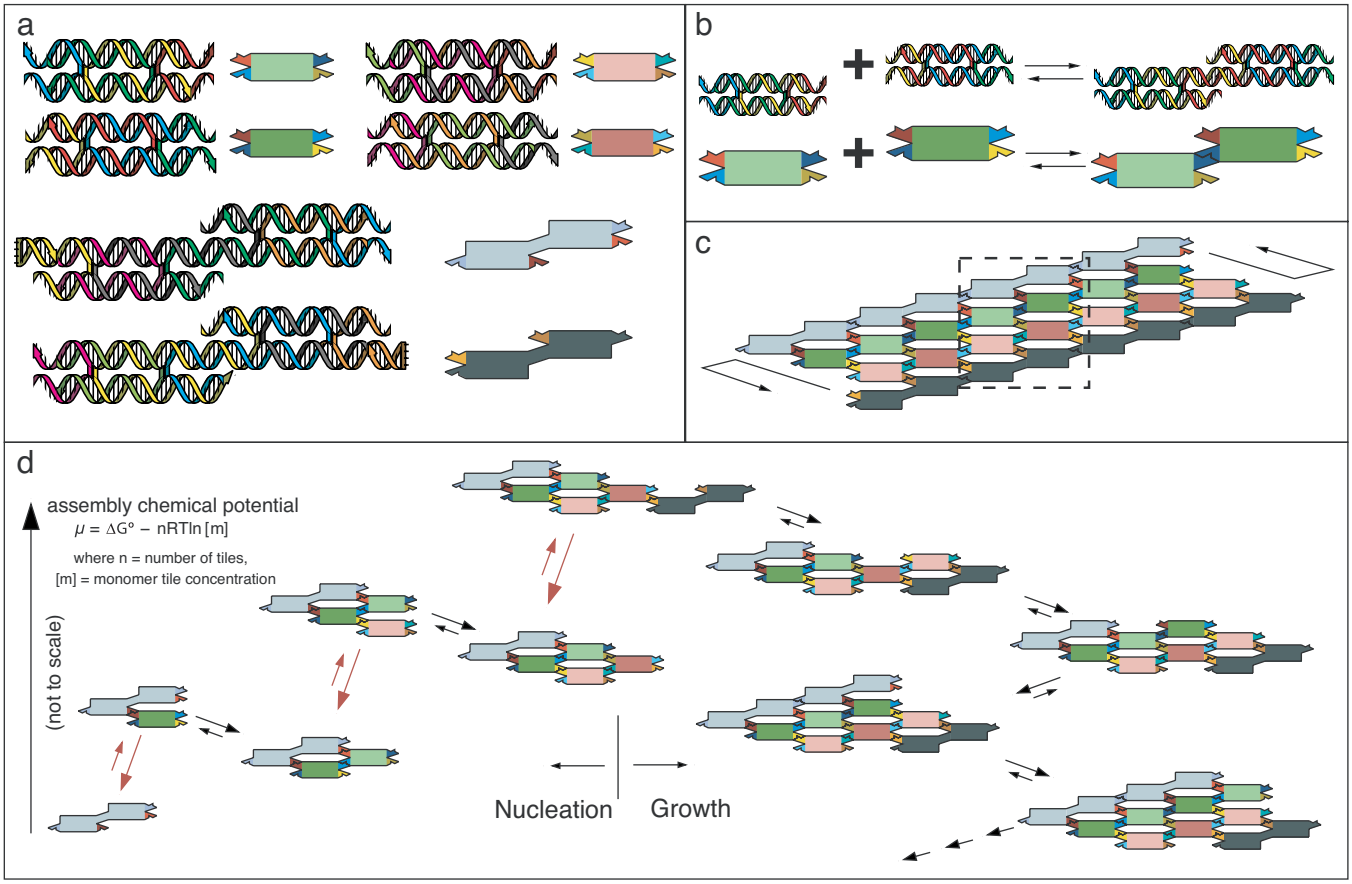

Fig. 1. Zig-zag ribbon design. (*a*) DNA tiles used to construct the four-tile-wide zig-zag ribbon, ZZ4. Single tiles (top two rows) each consist of four strands, and double tiles (bottom two rows) consist of six strands. Every strand has a unique sequence; colors distinguish the strands. Arrows indicate the 3′ (vs. 5′) ends of strands. Tile cores are double-stranded; their structures form because Watson–Crick complementary subsequences prefer to hybridize. Helix ends are single-stranded sticky ends that can hybridize to sticky ends on other tiles. Along the edges of the ribbon, the double tiles have noninteracting ends. Each tile has one of two orientations: The sticky ends on the top helix have either 3′ or 5′ ends. In subsequent diagrams, tiles are depicted by rectangle and claw diagrams. Colors of tile cores distinguish tile types. Claws with the same color represent complementary sticky ends. (*b*) Tiles bind by hybridization of their sticky ends. (*c*) ZZ4 tile structure. The dashed box encloses the six tile types in each repeating unit. Arrows show the zig-zag growth pattern of favorable assembly at each end of the ribbon. (*d*) Energetics of the standard sequence for nucleation and growth of ZZ4. Nucleation steps (at left) culminate in the critical nucleus (at top), followed by growth (at right). A monomer tile is added to the crystal at each reaction step. Large black arrows depict forward-biased reaction steps, and small red arrows depict unfavorable reaction steps.

growth and melting. Single-stranded DNA has a higher absorbance at 260 nm than does double-stranded DNA (hyperchromicity), so measured absorbance is proportional to the amount of unpaired DNA and slightly dependent on temperature (13). We recorded the absorbance of a ZZ4 sample at 50 nM as it was annealed from 90° to 15°C, held for 2 h, and melted back to 90°C at 0.13°C per minute (Fig. 3*a*). The resulting plot had two transitions: a reversible change between 70° and 45°C and a hysteretic transition between 40° and 15°C. Annealing and melting 50 nM of ZZ4 tiles without sticky ends (which cannot form ribbons) produced only the high-temperature, reversible transition, suggesting that tile formation and melting produced the reversible transition, whereas ribbon formation and melting produced the hysteretic transition. This interpretation is consistent with previously measured melting temperatures of DNA tiles and tile assemblies (14). We repeated this "temperature-ramp" experiment with ZZ3–ZZ6 at 25, 50, 100, and 200 nM (see SI Fig. S3).

Hysteresis signifies a kinetic barrier to nucleation. During the anneal of ZZ4, the solution became supersaturated (i.e., crystal formation became favorable) at ≈37°C (see below), but nucleation was not discernible for another 75 min, when the temperature had decreased to 27°C. To study how the amount of hysteresis changed with ribbon width and concentration, we compared absorbance traces produced by ribbons of different widths and concentrations (Fig. 3 *b* and *c*). The traces were normalized and the absorbance due to tile formation was subtracted, so that the onsets of formation and melting could be more clearly seen. We defined the formation temperature, T_f, as the first temperature at which the normalized absorbance reached 0.8, i.e., where significant growth is first observed. T_f decreased with concentration, but only slightly with ribbon width (Fig. 3*d*). The melting temperature, T_m, defined as the point at which the normalized absorbance equals 0.5 (i.e., the point at which half the ribbons are melted), did not change appreciably with width or concentration.

To determine whether these results were compatible with the designed pathways of zig-zag growth and nucleation, we constructed a simplified model of ribbon growth and nucleation, which we call the "standard sequence model." This model (Fig. 1*d*) considers a single prototypical assembly, A_n, containing n single or double tiles, thus ignoring the combinatorial number of possible species of each size. The model includes all reactions of the form

$$A_n + A_m \underset{k_r^{n,m}}{\overset{k_f^{n,m}}{\rightleftharpoons}} A_{n+m}$$

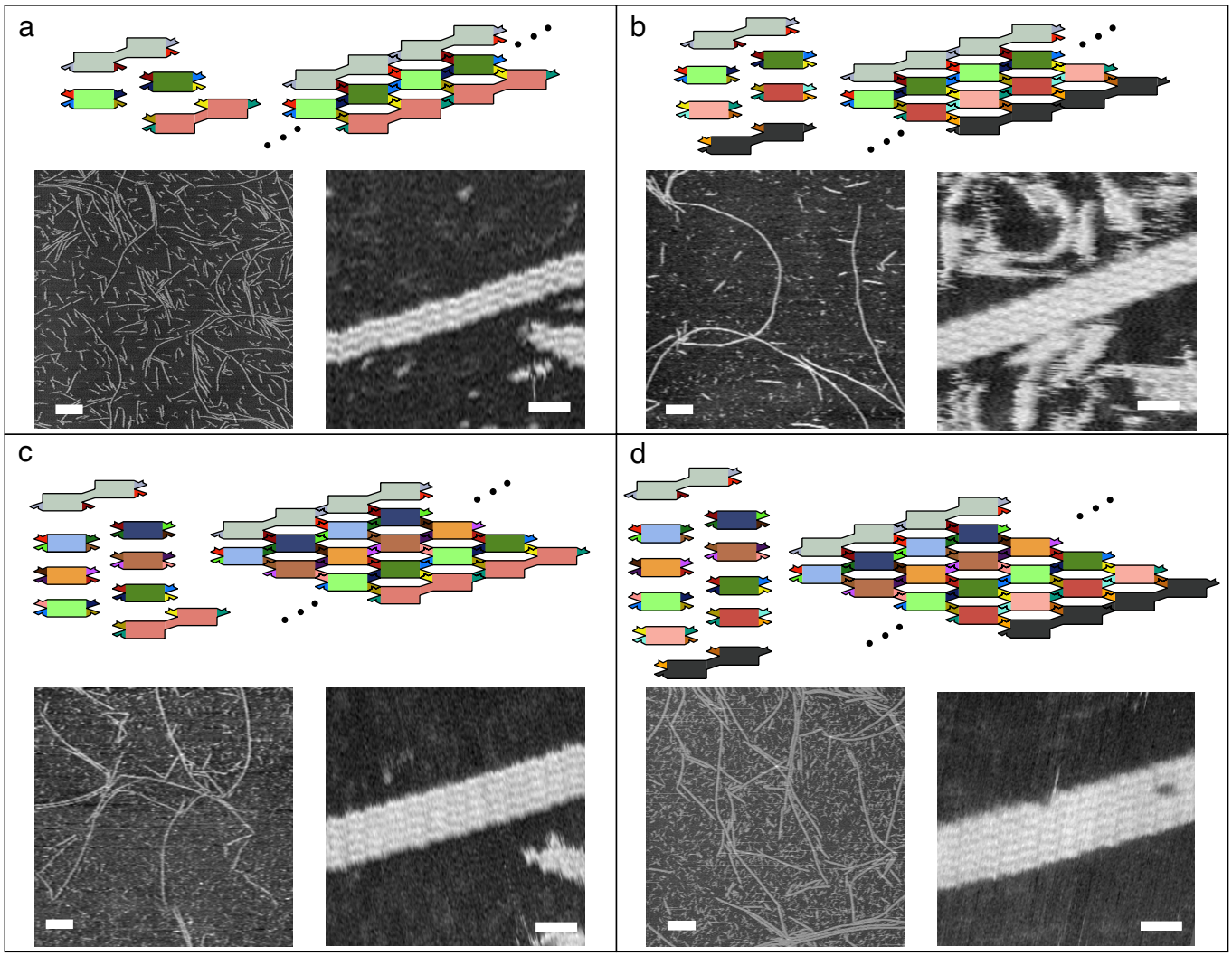

Fig. 2. Tile sets for ZZ3–ZZ6 (*a–d Upper*) and AFM images of ZZ3–ZZ6 (*a–d Lower*). Ribbons sometimes rip during sample deposition, leaving ribbon fragments stuck to the surface. [Scale bars: 500 nm (*Left*); 25 nm (*Right*).]

for $1 \leq n \leq m$, such that $n + m \leq M$, where M is the largest ribbon size modeled. M was limited by computation time to 100. The included reactions allow growth by monomer addition, as well as joining and internal scission of ribbons (15). To approximate the size dependence of the forward rate constant, we used $k_f^{n,m} = k_f = 10^6\ M^{-1}{\cdot}s^{-1}$ [typical for oligonucleotide hybridization (16)] for reactions involving a single tile or unnucleated assembly and $k_f^{n,m} = k_j = 35{,}000\ M^{-1}{\cdot}s^{-1}$ for two ribbons joining, which we measured experimentally (see *SI Appendix S3*). Thermodynamics determined the reverse rates: $k_r^{n,m} = k_f^{n,m} \exp\{-(\Delta G_n^\circ + \Delta G_m^\circ - \Delta G_{n+m}^\circ)/RT\}$. A_n has standard free energy $\Delta G_n^\circ = b_n\, \Delta G_{se}^\circ$, where b_n is the number of sticky end bonds in A_n (e.g., $b_6 = 7$ for the top assembly in Fig. 1*d*) and ΔG_{se}° is the free energy of hybridization for a single sticky end. We estimated or extrapolated these parameters from measured values. Assuming that the energetics for binding by multiple sticky ends are additive, we used $\Delta G_{se}^\circ = \frac{1}{2}(\Delta H^\circ - T\,\Delta S^\circ)$ where ΔH° and ΔS° are the enthalpy and entropy of a tile attaching to a ribbon by two sticky ends, as measured experimentally below.

The standard sequence simulations qualitatively reproduced most of the features of the absorbance traces (see SI Fig. S6), including the strong dependence of T_f on concentration and the steeper slope of the annealing curves for higher concentrations. The model also reproduced the lack of dependence of T_m on ribbon width but predicted an ≈3°C difference between T_m values at the highest and lowest concentrations, as would be expected from thermodynamics. This difference was not observed in experiments. At each concentration, both simulations and experiments showed similar T_f values for ZZ4–ZZ6 and a T_f for ZZ3 that was only slightly higher, even though the model assumed a different critical nucleus size for each ribbon width. This finding suggests that $T_m - T_f$ is not a measure of the height of the nucleation barrier under slight supersaturation. Rather, T_f in the temperature-ramp experiments is the temperature at which the nucleation barrier becomes insignificant (i.e., the solution becomes highly supersaturated).

Theoretical results (12), however, predict that nucleation rates decrease with ribbon width only under slightly supersaturated conditions, for which the critical size for nucleation is largest. Measuring nucleation rates under these conditions is challenging: Predicted nucleation rates are minuscule and exquisitely sensitive to both temperature and tile concentration. In two- or three-dimensional crystal growth, the rate of monomer depletion increases quickly after nucleation because the number of growth sites on a crystal increases as it grows. In contrast, a zig-zag ribbon has only two growth sites, regardless of its length, so the nucleation transition is not sharp. Furthermore, nucle-

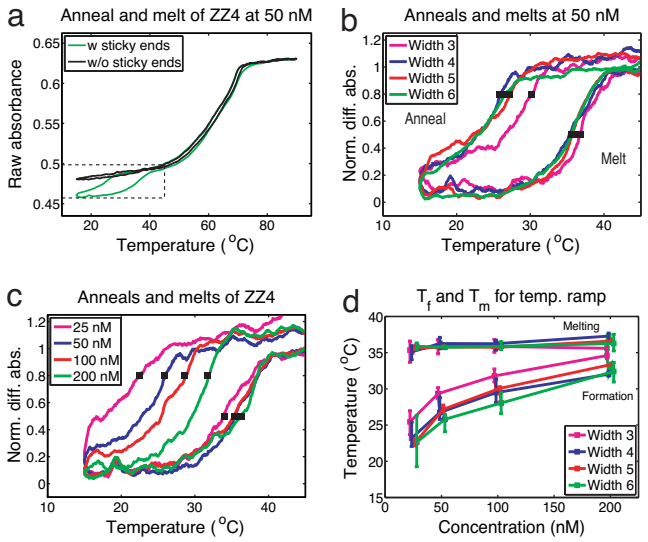

Fig. 3. Temperature-ramp anneals and melts. (*a*) Temperature-ramp experiment using zig-zag tiles with (green) and without (black) sticky ends. To adjust for cuvette and stoichiometry variations, the black trace was normalized so that the traces line up at 90°C and 42°C. The dashed box encloses the area shown in *b* and *c*. (*b*) Width dependence for ZZ3–ZZ6 at 50 nM. To approximate the fraction of unbound tiles, we normalized differential absorbance (the difference in absorbance between samples with and without sticky ends) to 0 at 15°C, where virtually all tiles were assembled into ribbons, and to 1 after melting to 42°C, where virtually all tiles were assumed to be unbound. Formation and melting temperatures are marked with black squares. (*c*) Concentration dependence for ZZ4 at 25, 50, 100, and 200 nM. Black squares as in *b*. (*d*) Formation and melting temperatures. Points are staggered so error bars are visible. Here and elsewhere, error bars are 95% confidence intervals, determined by bootstrapping, and are omitted for a few samples with insufficient data.

ation, growth, and ribbon joining (15) may occur simultaneously and on the same time scale, so that the absorbance changes resulting from continued formation of tiles and other nonidealities can be of the same magnitude as the absorbance changes that result from nucleation and growth.

These difficulties suggested that observation of ribbon growth at slightly supersaturated conditions over long periods of time would be necessary to observe differences in ribbon nucleation rates. So, for a range of target temperatures, T, we annealed the ribbons from 90°C to T and watched them grow (and approach equilibrium) for 24 h at that temperature. To determine the absorbance that corresponded to the equilibrium state at that temperature, we then annealed the ribbons to 15°C, held them there for 2 h, and then melted them back to the target temperature, where they were held for another 24 h. All temperature changes were made at the same speed as in the temperature-ramp experiments.

For these "temperature-hold" experiments, we held samples of ZZ3, ZZ4, and ZZ6 at target temperatures between 25° and 41°C. Absorbance traces from three ZZ4 experiments are shown in Fig. 4 *a–c*. At 39°C, above the melting temperature, there is no activity apart from an initial transient attributed to tile formation. At 33°C, there is a large barrier to nucleation: After 24 h, a significant separation still exists between the anneal and melt. At 25°C, there is a smaller kinetic barrier to nucleation: The absorbances of the anneal and melt holds converge within 24 h. The traces of all melt holds show no significant change after 6–12 h.

To study growth rates, the normalized absorbances at the beginning and end of each hold were plotted, as shown in Fig. 4 *d–i* (for 50 nM and 200 nM, see SI Fig. S7). Above 35–37°C, absorbance at the end of anneal and melt holds converged; at these temperatures no ribbons formed. At lower temperatures, the hysteresis remaining after 24 h (the gray areas in Fig. 4 *d–i*) increased with increasing ribbon width and decreasing concentration (see SI Fig. S8). The increase in hysteresis was a result of decreased formation temperatures; melting temperatures exhibited no measurable dependence on ribbon width and only a small dependence on concentration. (T_f and T_m for temperature-hold experiments were defined analogously as for temperature-ramp experiments. The values are different for the two types of experiments because they are kinetic, not equilibrium, measurements.) The low formation temperatures of wider ribbons means that seeded growth of wider ribbons can proceed over a wide temperature range without significant spontaneous nucleation.

Standard sequence simulations qualitatively reproduced the measured hysteresis, and the formation and melting temperatures, as a function of ribbon width and concentration (see SI Fig. S9). However, hysteresis was consistently more pronounced in simulation. As predicted by the model, ribbons at higher concentrations melted at higher temperatures. Equilibrium tile concentrations were achieved within a few hours of holding during the melt in the simulations. Because absorbance values also quickly reached their maximum values in all of the melt hold experiments, we inferred that equilibrium was achieved there as well.

We used the dependence of T_m on concentration to estimate the energetics of tile attachment. At T_m, the free energy of tile attachment, $\Delta G = \Delta G^\circ - nRT \ln([m])$ is 0, where $\Delta G^\circ = \Delta H^\circ - T\Delta S^\circ$ is the standard free energy of formation for a tile attaching by two sticky ends and $[m]$ is the concentration of unbound tiles of each type. We fit ΔH° and ΔS° by using a van't Hoff plot (17) of $1/T_m$ vs. $R \ln([m]_0/2)$, where $[m]_0$ is the initial tile concentration (Fig. 4*k*). The slope and intercept of this plot are ΔH° and ΔS°, respectively. Because the melting temperatures were not dependent on ribbon width, we pooled them for fitting and discarded the outlier (ZZ3, 100 nM). We measured $\Delta H^\circ = -102.4$ kcal/mol and $\Delta S^\circ = -0.300$ kcal/mol/K, which are comparable to average values (−99.7 kcal/mol and −0.276 kcal/mol/K) predicted by the nearest neighbor model of DNA hybridization (18, 19). At 37°C, our measurements (analyzed by bootstrapping) give $\Delta G^\circ = -9.43 \pm 0.21$ kcal/mol.

Accurate estimates of nucleation rates are difficult to obtain, as mentioned earlier, because zig-zag ribbons have temperature- and concentration-dependent critical nucleus sizes, and nucleation, growth, and joining happen on similar time scales. Nucleation rates therefore cannot be treated uniformly by classical nucleation theory (20). We instead used the temperature-hold results to directly estimate nucleation rates under conditions in which the tile concentration $[m]$ decreases only marginally, and thus the nucleation rate n_r remains approximately constant. We used

$$\frac{d[r]}{dt} = n_r - k_j[r][r], \qquad \frac{d[m]}{dt} = \frac{2}{N}(k_r[r] - k_f[m][r]),$$

where $[m]$ is the concentration of each tile type, $[r]$ is the concentration of ribbons ($[r] = 0$ at $t = 0$), k_f and $k_r = k_f e^{\Delta G^\circ/RT}$ are the rate constants for tile attachment and dissociation, and $N = 2w - 2$ is the number of tile types for a ribbon of width w. We used $k_f = 10^6\ \mathrm{M^{-1}\cdot s^{-1}}$ and $k_j = 35{,}000\ \mathrm{M^{-1}\cdot s^{-1}}$, as in the standard sequence model. [The significant joining rate explains why anneal holds in the hysteretic regime (e.g., Fig. 4*b*) stopped changing before reaching equilibrium: The nucleation rate was reduced because of its dependence on tile concentration, and few ribbon ends remained to deplete tile concentration.] To find n_r, we solved these equations using $[m]$ values at $t = 0$ and 24 h after annealing (see *SI Appendix S4*). We estimated $[m]$ linearly from absorbance by assuming that the dashed line corresponded to $[m]_0$ and that $[m]$ was at equilibrium at the end of the 24-h melt holds.

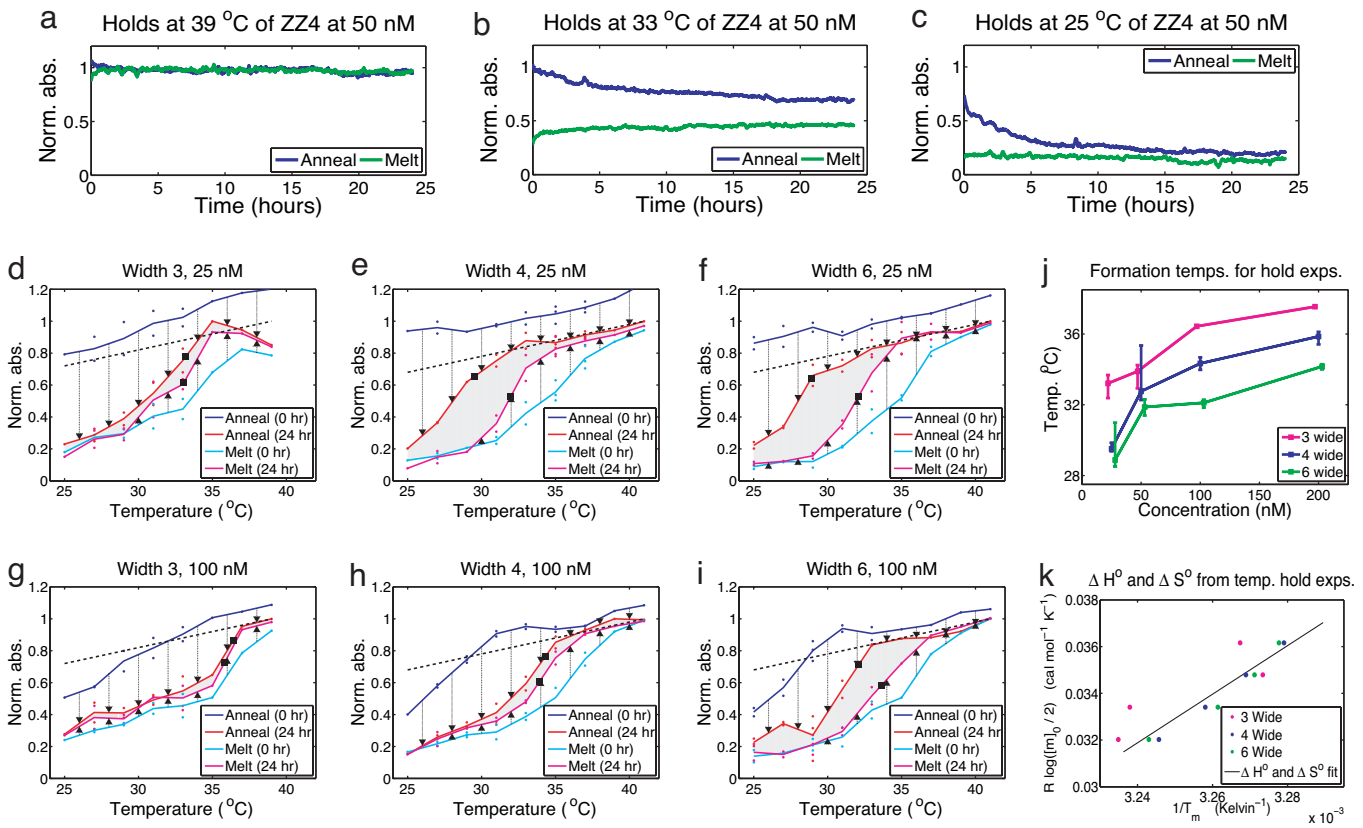

Fig. 4. Growth and melting at constant temperatures. (*a–c*) Growth and melting of 50 nM ZZ4 at three different temperatures. Absorbances are normalized as described in *d–i*. (*d–i*) Absorbances at the beginning (blue and cyan) and end (red and magenta) of temperature holds for anneals and melts, respectively. Points plot individual measurements, and lines connect averages for each temperature. Arrows indicate the direction of absorbance changes during holds. Gray regions show the hysteresis remaining after 24 h. Dashed lines indicate the estimated temperature-dependent absorbance for unbound tiles in solution. Black squares mark the formation and melting temperatures. Absorbances are normalized so that the largest absorbance after the 24-h anneal hold has value 1, and the absorbance at the end of the hold at 15°C has value 0. (*j*) Formation temperatures determined from temperature-hold experiments. (*k*) Determination of $\Delta H°$ and $\Delta S°$ from melting temperatures in temperature-hold experiments.

The nucleation rates at the melting temperature [where the supersaturation $\sigma = \ln([m]_0/[m]_{eq}) = \ln(2)$ is mild] are 3×10^{-7} nM/s, 10×10^{-7} nM/s, and $>70 \times 10^{-7}$ nM/s for ZZ6, ZZ4, and ZZ3 at 200 nM, respectively. Uncertainties from measurement error, estimation of k_f and k_j, and residual absorbance change due to continued tile formation render absolute values for n_r unreliable. However, for every concentration except 25 nM, the inferred nucleation rates decrease monotonically for wider ribbons, and this conclusion is robust to 10-fold changes in k_f and k_j. Although the measured decrease is not as strong as predicted, these results support theoretical predictions that nucleation rates should decrease with width (12).

Heterogeneous Nucleation of Ribbons. To test whether a segment of full-width ribbon could seed ribbon growth and remove the barrier to nucleation, we designed a seed for ZZ4 resembling two tile layers of the ribbon. The seed has the same sticky ends as ZZ4 on its right side (Fig. 1*c*), but its strands are woven so that it cannot easily fall apart into individual tiles (Fig. 5*a*). The seeds formed with ≈50% yield (Fig. 5*b*). They have a melting temperature of 62°C at the concentration at which the seeds were used, 2 nM (see SI Fig. S10), well above the melting temperatures of the ribbons.

To demonstrate seeded growth, two samples of ZZ4 were annealed from 90° to 40°C, at which point seeds were added to one of the samples. The samples were then cooled from 40° to 34°C and held at 34°C for 12 h. After the hold, the samples were cooled to 15°C and reheated to 34°C, and the temperature was held for another 12 h (Fig. 5*d*). By the onset of the hold, the distance between the anneal and melt absorbances was already smaller in the sample to which seeds were added. We propose that ribbons had by this time already nucleated on the seeds. The difference in the anneal and melt signals disappeared completely after a couple of hours for the seeded sample. Growth remained slow in the seedless sample.

Conclusions. The results here indicate that it is possible to engineer pathways of crystal growth by using rational design. More generally, our methods suggest a way to control the onset of a stage of self-assembly. Used recursively, this control can allow the ordered progress of multiple self-assembly reactions that together produce a complex structure.

Such kinetic control within self-assembly can be surprisingly powerful. It is theoretically possible to design a set of DNA tiles to assemble any computable shape or pattern (11, 21). This algorithmic crystal growth has been demonstrated experimentally (14, 22), but thus far spurious nucleation and errors during growth have resulted in poor yields. It may be possible to use the techniques developed here to reliably grow technologically relevant molecular structures with high yield, including crystals of exact rectangular dimension (23, 24) and the layout for a nanoscale demultiplexer circuit or memory circuit (25). Further, the control of nucleation in ribbons could allow single-molecule detection or the replication and evolution of crystal sequences encoded in ribbons (26).

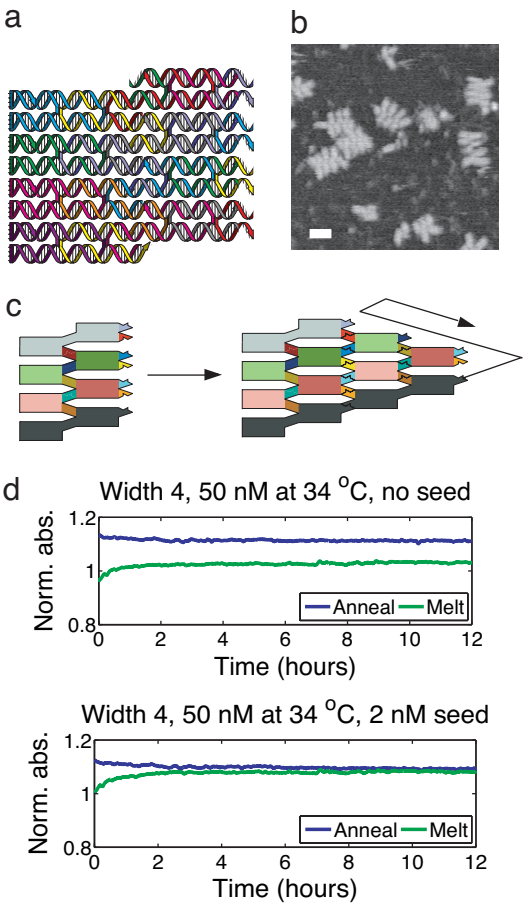

Fig. 5. Hysteresis in ribbon formation disappears when crystal seeds are present. (*a*) A designed nucleus for ZZ4. The size of the helical regions and placement of crossover points are the same as in the tile lattice. (*b*) AFM image of the crystal seeds. (Scale bar: 25 nm.) Both intact and incomplete structures are seen. (*c*) Putative growth from a crystal seed: at every step, tiles can bind favorably (by two sticky ends) to produce the structure shown at right, which can then grow through zig-zag growth. (*d*) Hysteresis of 50 nM ZZ4 with (*Lower*) and without (*Upper*) crystal seeds at 34°C over 12 h. The higher absorbance during the melt in the sample with seeds is due to the added material.

The approach described here for control over nucleation is potentially applicable to other organic and macromolecular crystals if sufficient control over intermolecular interactions can be achieved by design. Generalization to two- or three-dimensional crystal growth is also possible (27, 28). Control over nucleation of supramolecular assemblies can also be achieved by conformational changes (29) or by energy-consuming enzymatic activity (30). These methods, along with the work described here, present the engineer of complex self-assembly processes with a rich design space.

Materials and Methods

Design. DAO-E tiles (Fig. 1 *a* and *b*) were used to construct ribbons (7). Sequences for the double-stranded tile regions were either those used previously (14) or those designed by computer using sequence symmetry minimization (31, 32), a technique that selects sequences with minimal undesired intramolecular and intermolecular interactions. Sticky end sequences were designed so that binding strengths between pairs of complementary ends were similar and binding energies between noncomplementary ends were minimized. Binding energies were estimated by using the nearest neighbor model (17).

Experiments. Reactions were performed in Tris-Acetate EDTA buffer containing 12.5 mM hydrous $Mg(CH_3COO)_2$. Nondenaturing gel electrophoresis showed that all tiles formed with at least 80% yield, and crystal seeds formed with ≈50% yield. Kinetics and temperature-dependent measurements of UV absorbance were performed using an AVIV 14DS spectrophotometer (AVIV Biomedical, Lakewood, NJ) equipped with a computer-controlled temperature bath. AFM was performed on a Digital Instruments Nanoscope III (Veeco Metrology, Santa Barbara, CA) in fluid tapping mode, using NP-S tips. Samples in Fig. 2 were prepared by pipetting 40 μl of buffer followed by 3 μl of sample onto freshly cleaved mica. The sample in Fig. 5*b* used buffer containing 5 mM $NiCl_2$ instead of $Mg(CH_3COO)_2$.

Design and experimental details are given in *SI Appendix S1*.

We thank Paul Rothemund, Bernie Yurke, Peng Yin, Ho-Lin Chen, Rizal Hariadi, Rick Flagan, and Rob Barish for insightful discussions and encouragement. This work was supported by National Aeronautics and Space Administration Astrobiology Grant NNG06GA50G and National Science Foundation Grant NANO/CCF-0432193.

1. Welch MD, Mullins RD (2002) *Annu Rev Cell Dev Biol* 18:247–288.
2. Sept D, McCammon JA (2001) *Biophys J* 81:867–874.
3. Moritz M, Braunfeld MB, Sedat JW, Alberts B, Agard DA (1995) *Nature* 378:638–840.
4. Aldrige P, Hughes KT (2002) *Curr Opin Microbiol* 5:160–165.
5. Fu T, Seeman NC (1993) *Biochemistry* 32:3211–3220.
6. Li X, Yang X, Qi J, Seeman NC (1996) *J Am Chem Soc* 118:6131–6140.
7. Winfree E, Liu F, Wenzler LA, Seeman NC (1998) *Nature* 394:539–544.
8. LaBean TH, Yan H, Kopatsch J, Liu F, Winfree E, Reif JH, Seeman NC (1999) *J Am Chem Soc* 122:1848–1860.
9. Rothemund PWK, Ekani-Nkodo A, Papadakis N, Kumar A, Fygenson DK, Winfree E (2004) *J Am Chem Soc* 126:16344–16352.
10. Mathieu F, Liao S, Kopatsch J, Wang T, Mao C, Seeman NC (2005) *Nano Lett* 5:661–665.
11. Winfree E (1995) in *DNA Based Computers* (Springer, Berlin), pp 199–221.
12. Schulman R, Winfree E (2006), arXiv:cond-mat/0607317. Available at http://arxiv.org/abs/cond-mat/0607317.
13. Marky LA, Breslauer KJ (1987) *Biopolymers* 26:1601–1620.
14. Rothemund PWK, Papadakis N, Winfree E (2004) *PLOS Biol* 2:424–436.
15. Ekani-Nkodo A, Kumar A, Kuchnir-Fygenson DK (2004) *Phys Rev Lett* 93:268301.
16. Wetmur JG (1991) *Crit Rev Biochem Mol Biol* 36:227–259.
17. Dill KA, Bromberg S, Stigter D (2002) *Molecular Driving Forces* (Garland, New York).
18. SantaLucia J, Jr (1998) *Proc Natl Acad Sci USA* 95:1460–1465.
19. Zuker M (2003) *Nucleic Acids Res* 31:3406–3415.
20. Davey R, Garside J (2000) *From Molecules to Crystallizers* (Oxford Univ Press, Oxford).
21. Soloveichik D, Winfree E (2004) in *DNA Computing 10* (Springer, Berlin), pp 344–354.
22. Barish RD, Rothemund PWK, Winfree E (2005) *Nano Lett* 5:2586–2592.
23. Rothemund PWK, Winfree E (2000) in *Proceedings of the 32nd Annual Association for Computing Machinery Symposium on the Theory of Computing* (Assoc Computing Machinery, New York), pp 459–468.
24. Adleman LM, Cheng Q, Goel A, Huang M (2001) in *Proceedings of the 33rd Annual Association for Computing Machinery Symposium on the Theory of Computing* (Assoc Computing Machinery, New York), pp 740–748.
25. Cook M, Rothemund PWK, Winfree E (2003) in *DNA Computing 9* (Springer, Berlin), pp 91–107.
26. Schulman R, Winfree E (2005) in *Proceedings of the Eighth European Conference on Advances in Artificial Life*, eds Capcarrère MS, Freitas AA, Bentley PJ, Johnson CG, Timmis J (Springer, Berlin), Vol 3630, pp 734–743.
27. Liu Y, Ke Y, Yan H (2005) *J Am Chem Soc* 127:17140–17141.
28. Rothemund PWK (2006) *Nature* 440:297–302.
29. Dirks RM, Pierce NA (2004) *Proc Natl Acad Sci USA* 101:15275–15278.
30. Bar-Ziv R, Tlusty T, Libchaber A (2002) *Proc Natl Acad Sci USA* 99:11589–11592.
31. Seeman NC (1990) *J Biomol Struct Dyn* 8:573–581.
32. Dirks RM, Lin L, Winfree E, Pierce NA (2004) *Nucleic Acids Res* 32:1392–1403.